Reactivity of Ru oxides with air radiolysis products investigated by theoretical calculations

Faoulat Miradji, Souvi M. O. Sidi, Laurent Cantrel, Florent Louis, Valérie Vallet

Reactivity of Ru oxides with air radiolysis products investigated by theoretical calculations

Faoulat Miradji,[1,2,3,4] Sidi M. O. Souvi,[1,3] Laurent Cantrel,[1,3] Florent Louis,[2,3] and Valérie Vallet[4]

[1] *Institut de Radioprotection et de Sûreté Nucléaire (IRSN) PSN-RES, Cadarache, St Paul Lez Durance, 13115, France*

[2] *Univ. Lille, CNRS, UMR 8522 - PC2A - Physicochimie des Processus de Combustion et de l'Atmosphère, F-59000 Lille, France*

[3] *Laboratoire de Recherche Commun IRSN-CNRS-Lille1 Cinétique Chimique, Combustion, Réactivité (C^3R), Cadarache, Saint Paul Lez Durance,13115, France*

[4] *Univ. Lille, CNRS, UMR 8523 - PhLAM - Physique des Lasers Atomes et Molécules, F-59000 Lille, France*

(Dated: Received: November 8, 2021)

Quantitative predictions of the release of volatile radiocontaminants of ruthenium (Ru) in the environment from either nuclear power plants (NPP) or fuel recycling accidents present significant uncertainties while estimated by severe accidents nuclear analysis codes. Observations of Ru from either experimental or modeling works suggest that the main limitations relate to the poor evaluation of the kinetics of gaseous Ru in the form of RuO_3 and RuO_4. This work presents relativistic correlated quantum chemical calculations performed to determine the possible reactions pathways leading to the formation of gaseous Ru oxides under NPP severe accident conditions, as a result of reactions of RuO_2 gaseous with air radiolysis products, namely nitrous and nitrogen oxides. The geometries of the relevant species were optimized with the TPSSh-5%HF functional of the density, while the total electronic energies were computed at the CCSD(T) level with extrapolations to the complete basis set CBS limit. The reaction pathways were fully characterized by localizing the transition states and all intermediate structures using the internal coordinate reaction algorithm (IRC). The rate constants were determined over the temperature range 250–2500 K. It is revealed that the less kinetically limiting pathway to form Ru gaseous fraction is the oxidation of Ru by nitrogen oxide, corroborating experimental observations.

Keywords: Severe accident; Ruthenium transport; Reactor cooling system; Kinetics; Quantum chemistry

INTRODUCTION

The prevention of the radiological consequences of ruthenium release in the environment, implying the evaluation of its source term, is crucial for nuclear safety, as ruthenium-containing compounds present severe sanitary issues due to ^{103}Ru and ^{106}Ru isotopes, considered as short and medium radio contaminants like ^{131}I and ^{137}Cs [1]. Such a release may occur mostly in the event of a nuclear power plant (NPP) severe accident (SA) like the Three Mile Island or the Chernobyl ones [2, 3], but sometimes from nuclear fuel recycling plant as observed lately through the Ural accident provoking a release of ruthenium ^{106}Ru over European countries [4, 5]. Literature review on Ru transport studies reported that Ru volatilization can be influenced by humidity, temperature, and air flow rate in the Reactor Coolant System (RCS) [6, 7] during a severe accident. The interactions with other elements released from the fuel may also impact the chemical composition and possibly the quantity of transported Ru [8]. The mechanisms involved in the ruthenium release are still not well characterized and implemented in SA analysis codes [9]. The volatile form of Ru is ruthenium tetroxide that can exist in oxidizing atmosphere and which is not easy to trap by usual filters [10] but can be thermally reduced into non-volatile RuO_2 form. Chemical reactivity of gaseous RuO_4 has to be modeled in order to better assess potential releases in the frame of a nuclear accident. In a previous theoretical work, we have used relativistic correlated quantum chemical methods to consolidate and extend Ru thermodynamics database [11, 12]. It was revealed that thermodynamic properties of Ru compounds in SA databases agree with our theoretical calculations. Thence, a possible explanation for the observed discrepancies between the simulated and experimental amounts of Ru transported fractions, might be related to kinetic limitations in the formation of gaseous ruthenium molecules [13].

Thus, several research programs are currently led to improve knowledge on Ru transport schemes [6, 14–17]. Among them, the Technical Research Centre of Finland (Teknologian tutkimuskeskus, VTT) program studied ruthenium transport in humid atmosphere with air radiolysis products [6, 16, 17]. The radiation of the atmosphere in the reactor vessel is thought to occur under an NPP SA leading in particular to the formation of air radiolysis products like nitrogen and/or nitrous oxides [18, 19]. The results of the VTT program underlined that the major part of Ru released from the crucible was deposited inside the apparatus. The transported Ru fractions were in condensed and gaseous forms. The aerosols were identified as RuO_2 and the gaseous form was identified as RuO_4, according to instrumental neutron activation analysis. As it was found that air radiolysis products enhance the fraction of gaseous Ru at the outlet of the experimental set-up, we decided to launch quantum chemical calculations to determine reaction pathways and their kinetic parameters that lead to the formation of the gaseous fraction of ruthenium (RuO_3 and RuO_4 compounds, likely to be formed under experimen-

tal conditions [12]), with air radiolysis products N_2O and NO_2, according to the following chemical reactions:

$$RuO_2 + N_2O \longrightarrow RuO_3 + N_2 \quad (1)$$
$$RuO_3 + N_2O \longrightarrow RuO_4 + N_2 \quad (2)$$
$$RuO_2 + NO_2 \longrightarrow RuO_3 + NO \quad (3)$$
$$RuO_3 + NO_2 \longrightarrow RuO_4 + NO. \quad (4)$$

COMPUTATIONAL METHODOLOGY

Structural properties and energetics

The geometries of all stationary points for the relevant chemical reactions were optimized using the TPSSh-5%HF density functional [20], validated in our previous works to obtain thermodynamic properties of Ruthenium oxides and oxyhydroxides [11, 12]. In our calculations, the N, O, and H atoms are described with augmented correlation consistent polarized triple zeta aug-cc-pVTZ (noted aVTZ) basis sets [21]. The ruthenium atom is described by the aug-cc-pVTZ-PP basis set of Peterson *et al.* [22], which incorporates a relativistic pseudo-potential that accounts for scalar relativistic effects in the Ru atom. Vibrational frequencies and zero-point energies (ZPE) were determined at the same level of theory as the geometries. When a transition state structure has been located on the potential energy surface, intrinsic reaction coordinates calculations (IRC) have been performed using the algorithm implemented in the Gaussian09 RevC.01 software [23] to find the associated molecular complexes on the reactant (MCR) and product (MCP) sides.

In a second step, to obtain accurate potential energies of all stationary points, single and double coupled cluster with inclusion of a perturbative estimation for triple excitation (CCSD(T)) [24, 25] calculations were performed with the MOLPRO quantum chemistry package Version 2015.1 [26, 27]. The full valence (oxygen 2s and 2p and ruthenium 5s and 4d) orbitals of Ru compounds were correlated in the CCSD(T) calculations. The total energies computed with triple-ζ ($n = 3$), and quadruple-ζ ($n = 4$) basis set qualities were extrapolated to the complete basis set (CBS) limit using a two-fold scheme to extrapolate Hartree-Fock energies [28, 29] and correlation energies [30], as described in our previous works [11, 12]. The use of DFT optimized geometries combined with CCSD(T) single point energy calculations was portrayed in a recent work by Fang *et al.* [31] to study small Ru clusters with water, enhancing the appropriateness of such methodology to evaluate Ru related compounds thermochemistry.

Regarding spin-orbit (SO) coupling, it was found in our previous investigation [11] that SO contributions amounted to 16, 10 and 0.75 kJ mol^{-1} for Ru, RuO, and RuO_2 compounds, respectively. In this study, we don't expect SO contributions to exceed that found for the Ru atom, and as the ground state wave functions have low spin contamination, we can safely assume that SO corrections cancel when considering reaction and activation energies.

Rate constants

The rate constants of the reactions were calculated using the direct transition state approach, as applied in our previous work [32]. The direct mechanism considers the reaction from the reactants to the products, and the formation of the pre-reactive complex (MCR) is disregarded. The canonical Transition State Theory (TST) [33–39] was applied to calculate the temperature dependence of the rate constant for the direct mechanism, k_{direct}, as follows:

$$k_{direct}(T) = \Gamma(T) \times \frac{k_B T}{h} \times \frac{Q_{TS}(T)}{Q_A(T) Q_B(T)} \times \exp\left(-\frac{E_{TS} - E_A - E_B}{k_B T}\right) \quad (5)$$

where $\Gamma(T)$ represents the transmission coefficient used for the tunneling correction at temperature T, and k_B and h are the Boltzmann and Planck constants, respectively. $Q_A(T)$, $Q_B(T)$, and $Q_{TS}(T)$ are the total partition functions of A, B, and the TS at the temperature T, respectively. E_A, E_B, and E_{TS} are the total energies at 0 K including the zero-point energies.

The GPOP program [40] was used to extract information from the Gaussian output files to estimate the Eckart tunneling corrections and to perform the rate constant calculations over the temperature range of interest, 250–2500 K. The structural properties, energetics and kinetic parameters of selected reactions pathways are discussed in the next subsections.

RESULTS AND DISCUSSION

Reaction coordinates with N_2O

The reaction coordinates involving oxidation of RuO_2 by N_2O are displayed in Fig. 1 for the formation of RuO_3 and Fig. 2 for the formation of RuO_4. The corresponding geometrical parameters and ZPE corrections are listed in Tables I, and II, respectively.

The TS(1) structure corresponding to the formation of RuO_3 features a one-step mechanism with the breaking of the N−O bond, stretched up to 1.351 Å from its equilibrium value in N_2O, to form the third Ru-O bond, equal to 1.934 Å. This bond length is typical of ionic bonding, as observed between hydroxyl ligands and Ru oxides in

TABLE I: Structural parameters (bond lengths r in Å), imaginary vibrational frequency (cm^{-1}), and ZPE (kJ mol^{-1}), for the transition state and molecular complexes calculated at the TPSSh-5%HF/aVTZ level of theory, involved in the reaction $RuO_2 + N_2O \longrightarrow RuO_3 + N_2$

Parameters	MCR(1)	TS(1)	MCP(1)
r(N−N)	1.124	1.128	1.097
r(N−O)	1.222	1.351	
r(Ru−O_{N_2O})	2.126	1.934	
r(Ru−O)	1.680	1.676	1.685
r(Ru−N_{N_2})			4.527
θ(N−N−O)	173.4	148.8	
θ(O−Ru−O_{N_2O})	109.8	113.9	
θ(O−Ru−O)	140.5	133.9	120.0
ν_{im}		590**i**	
ZPE	43.94	49.96	36.20

TABLE II: Structural parameters (bond lengths r in Å) imaginary vibrational frequency (cm^{-1}), and ZPE (kJ mol^{-1}), for the transition state and molecular complexes calculated at the TPSSh-5%HF/aVTZ level of theory, involved in the reaction $RuO_3 + N_2O \longrightarrow RuO_4 + N_2$

Parameter	MCR(2)	TS(2)	MCP(2)
r(N−N)	1.130	1.121	1.098
r(N−O)	1.187	1.262	
r(Ru−O_{N_2O})	4.986	2.103	
r(Ru−O)	1. 684	1.762-1.688	1.684
r(Ru−N)			4.020
θ(N−N−O)	180	159.4	
θ(O−Ru−O_{N_2O})	118.8	113.1-118.1	
θ(O−Ru−O)	120.0	108.1	109.3-109.5
ν_{im}		572**i**	
ZPE	50.73	49.96	48.62

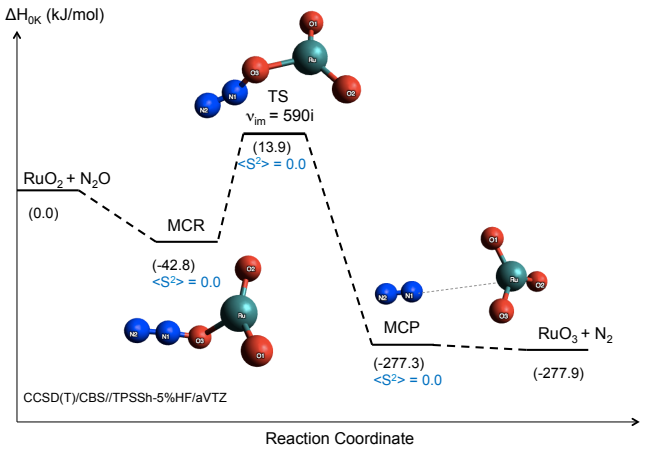

FIG. 1: Reaction coordinate at 0 K of the $RuO_2 + N_2O \longrightarrow RuO_3 + N_2$ reaction, including ZPE, calculated at the CCSD(T)/CBS//TPSSh-5%HF/aVTZ level of theory, displayed along with schematic representations of the intermediate species involved.

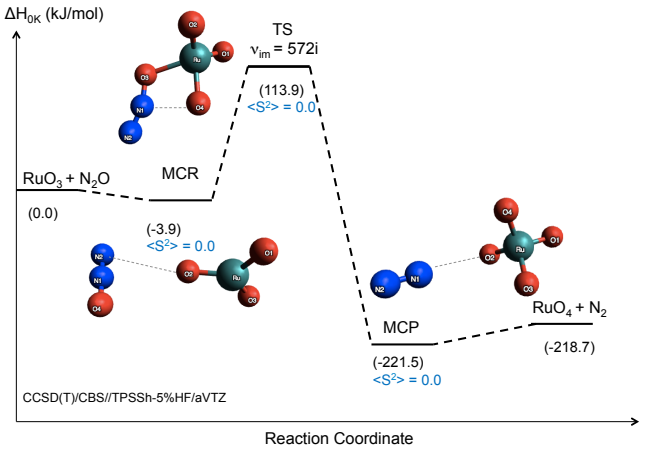

FIG. 2: Reaction coordinate at 0 K of the $RuO_3 + N_2O \longrightarrow RuO_4 + N_2$ reaction, including ZPE, calculated at the CCSD(T)/CBS//TPSSh-5%HF/aVTZ level of theory, displayed along with schematic representations of the intermediate species involved.

our previous work [12]. The value of the RuO_2 bond angle decreases to favor a pyramidal structure leading to the formation of RuO_3.

In the TS(2) structure leading to the formation of RuO_4, the elongation of N−O bond distance is only 0.075 Å, much closer to the equilibrium reactant structure than in the previous TS. The bond angles and bond distances shrink from their equilibrium values, to form the tetrahedral RuO_4 structure. This reaction involves the creation of the fourth Ru−O bond with a length of 2.101 Å, sharing fewer electrons between Ru and O_{N_2O} atoms compared to its counterpart in the previous TS. A bridge between O_{RuO_3} and N_{N_2O} is also observed, measuring 2.258 Å, indicating that the formation of RuO_4 originates from a large orbital mixing between the reactants.

The connections between TS(2) and both the $RuO_2\cdots N_2O$ reactant complex (MCR(1)) and $RuO_3\cdots N_2$ product complex (MCP(1)) have been established in both forward and backward directions via IRC calculations at the TPSSh-5%HF/aVTZ level of theory. The ionic interaction (2.126 Å) between O_{N_2O} and the Ru atom stabilizes the RuO_2 and N_2O reactants to form the MCR(1) complex. In reaction 2, the structure of the MCR involves a very weak interaction of the Van der Waals type (4.986 Å), leaving the bond angles and bond distances similar to those in RuO_3 and N_2O reactant species. Such interactions are also observed in MCP systems for both reactions, where the Ru−N bond length is equal to 4.527 and 4.020 Å, for $RuO_3\cdots N_2$ and $RuO_4\cdots N_2$ complexes, respectively. The relative enthalpies at 0 K in the reaction coordinate curve reveal that the reaction between N_2O and RuO_2 has to overcome a barrier of about 14 kJ mol^{-1} to form the N_2 and RuO_3 products. The MCR(1) is

TABLE III: Structural parameters (bond lengths r in Å) imaginary vibrational frequency (cm^{-1}), and ZPE (kJ mol^{-1}), for the transition state and molecular complexes calculated at the TPSSh-5%HF/aVTZ level of theory, involved in the reaction $RuO_2 + NO_2 \longrightarrow RuO_3 + NO$

Parameters	MCR(3)	TS(3)	MCP(3)
r(N−O)	1.191	1.175	1.145
r(Ru−O_{NO_2})	1.316	1.866–1.988	
r(Ru−O_{NO})			1.693
r(Ru−O)	1.648	1.661	1.673–1.847
θ(O−N−O)	124.8	124.7	110.8
θ(O−Ru−O_{NO_2})	93.0	72.9	
θ(O−Ru−O_{NO})			114.8
θ(O−Ru−O)		139.7	128.8
ν_{im}		477**i**	
ZPE	46.8	39.8	38.2

stabilized by $\sim$ 43 kJ mol^{-1} with respect to the reactants. The MCP is similar to the products, and lies only 0.6 kJ mol^{-1} below the product energy limit.

For the reaction 2 (See Fig. 2), the transition state is located above reactants with an important vibrationally adiabatic barrier of about 113.9 kJ mol^{-1} by comparison to the one found for reaction 1a (13.9 kJ mol^{-1}).The pro- and post-reactive complexes are similar to the reactants and products, respectively, differing only by $\sim$ 4 kJ mol^{-1}.

Reaction coordinates with NO_2

We now turn to presenting the reaction coordinates corresponding to NO_2 oxidation. The optimized geometry parameters for NO (r(N−O) $\sim$1.154 Å) and NO_2 (r(N−O) $\sim$1.199 Å; θ(O−N−O)$\sim$134.2°) are in good agreement with their experimental counterparts (r(N−O)$\sim$1.514 Å for NO [41]; r(N-O)$\sim$1.193 Å; θ(O-N-O)$\sim$134.1° for NO_2 [42]).

The structures of intermediate species involved in the formation of RuO_3 in reaction 3 and relative enthalpies at 0 K are shown in Fig. 3. For the formation of RuO_4, two reaction mechanisms, noted paths 1 and 2, were explored and are illustrated in Fig. 4 and Fig. 5, respectively. Path 1 showcases nitrogen oxide forming a bond with one of ruthenium trioxide. Path 2 investigates Ru element forming a bond directly with the oxygen of nitrogen oxide. The corresponding geometrical parameters are reported in Tables III, IV, and V.

The investigation of reaction 3 pathway was conducted by approaching NO_2 species to RuO_2 oxide. The most stable potential energy led to an MCR(3) complex adopting a ring-like structure in which RuO_2 and NO_2 interact through two symmetric covalent bonds (1.316 Å) between O_{RuO_2}−N_{NO_2}, and Ru−O_{NO_2}, forming a terminal nitrate bidentate like structure. However, the N−O

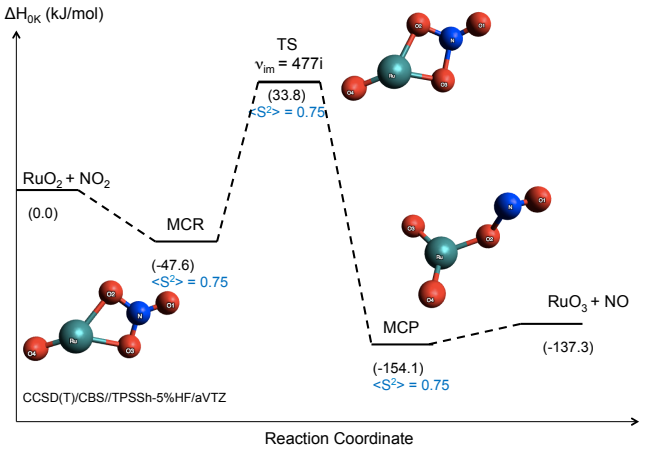

FIG. 3: Reaction coordinate at 0 K calculated at the CCSD(T)/CBS//TPSSh-5%HF/aVTZ level of theory for reaction $RuO_2 + NO_2 \longrightarrow RuO_3 + NO$ with schematic representations of the intermediate species involved.

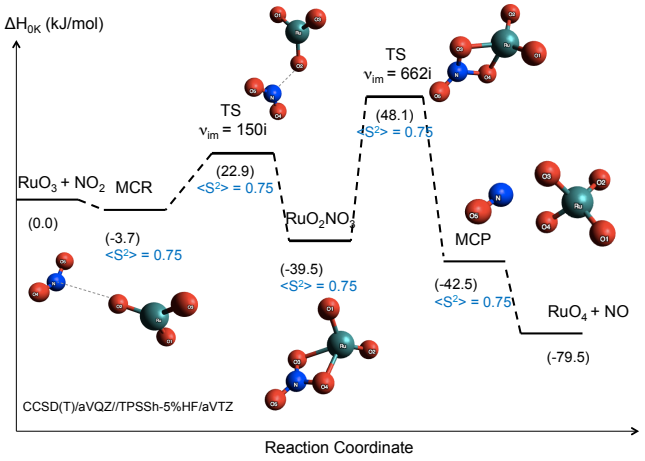

FIG. 4: Reaction coordinate at 0 K calculated at the CCSD(T)/CBS//TPSSh-5%HF/aVTZ level of theory for path 1 in reaction $RuO_3 + NO_2 \longrightarrow RuO_4 + NO$, with schematic representations of the intermediate species involved.

bond distance, 1.191 Å remains similar to its counterparts in nitrogen dioxide (1.199 Å). Such observation is consistent with our previous work [11] which underlined competitive effects between an increase of oxide bond lengths and increase of oxide charges (in this case on O atom) which kept the oxide bonds similar. In addition, the analysis of spin density of MCR(3) (Fig. S2a of the ESI) compound shows that the spin density of NO_2 is transferred to Ru oxide, acknowledging a chemisorbed like structure, consistent within Lee *et al.* work [43], who observed chemisorbed-like structures for group IV $(MO_2)_n$, M=Ti, Zr, Hf dioxides nanoclusters from DFT and CCSD(T) calculations. The bond angle θ(O-N-O) decreases by ca. 9°. These results suggest that the RuO_2

TABLE IV: Structural parameters (bond lengths r in Å), imaginary vibrational frequency (cm^{-1}), and ZPE (kJ mol^{-1}), for the transition state and molecular complexes calculated at the TPSSh-5%HF/aVTZ level of theory, involved in path 1 for the reaction $RuO_3 + NO_2 \longrightarrow RuO_4 + NO$

Parameters	MCR(4-P1)	TS1(4-P1)	RuO_2NO_3	TS2(4-P1)	MCP(4-P1)
r(N−O)	1.197–1.200	1.184–1.188	1.184	1.183	1.125
r(Ru−O_{NO_2})	4.008	3.523	2.109	1.910	
r(Ru−O)	1.687	1.686 -1.727	1.689	1.693	1.694–1.735
r(N−O_{RuO_3})	2.893	2.13	1.134	1.402–1.483	
r(N−O_{RuO_4})					2.198
θ(O−N−O)	134.7	137.6	124.2	125.3	
θ(O−Ru−O_{NO_2})	104.0	103.8	62.3	70.9	
θ(O_{RuO_4}−N−O_{RuO_4})					71.7
θ(O−Ru−O)	119.8–120.3	117.9–123.4	102.6–124.8	109.7–120.9	95.7–115.7
ν_{im}		150**i**		662**i**	
ZPE	44.6	47.2	54.2	48.0	

TABLE V: Structural parameters (bond lengths r are Å) imaginary vibrational frequency (cm^{-1}), and ZPE (kJ mol^{-1}), for the transition states and molecular complexes calculated at the TPSSh-5%HF/aVTZ level of theory, involved in path 2 for the reaction $RuO_3 + NO_2 \longrightarrow RuO_4 + NO$

Parameters	MCR(4-P2)	TS1(4-P2)	RuO_3NO_2	TS2(4-P2)	MCP(4-P2)
r(N−O)	1.178-1.421	1.204-1.313	1.133	1.126	1.137
r(Ru−O_{NO_2})	1.931	2.028	1.843		
r(O_{RuO_4}−N_{NO})			1.668	1.796	2.358
r(Ru−O)	1.688-1.725	1.685-1.723	1.692-1.733	1.693-1.728	1.696-1.711
θ(O−N−O)	114.8	114.5	115.0		
θ(O−Ru−O_{NO_2})	109.3	115.9	100.6		
θ(Ru−O−N_{NO})			123.9	119.7	114.9
θ(O−Ru−O)	109.7-121.5	108.9-120.9	108.0-120.1	107.7-116.7	106.7-110.7
ν_{im}		209**i**		229**i**	
ZPE	47.1	47.5	47.4	45.6	46.2

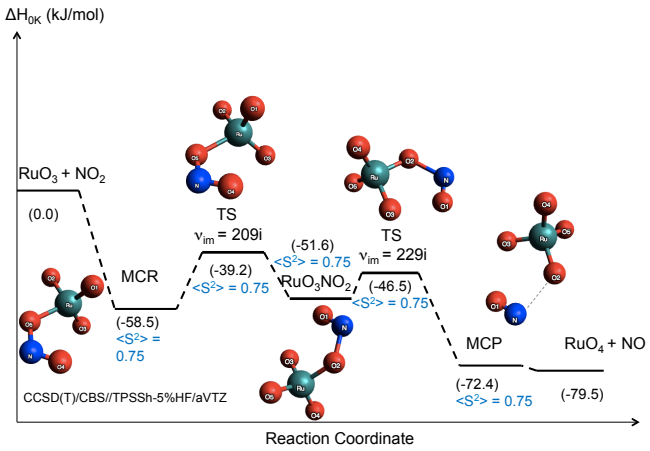

FIG. 5: Reaction coordinate at 0 K calculated at the CCSD(T)/CBS//TPSSh-5%HF/aVTZ level of theory for path 2 in reaction $RuO_3 + NO_2 \longrightarrow RuO_4 + NO$, with schematic representations of the intermediate species involved.

electrons are the ones mostly involved in these two symmetric bonds in this complex; this is confirmed by the fact that the Ru−O bond lengths are shorter, 1.648 Å, and the θ(O−Ru−O) bond angle is more acute, 140.2°, than in the RuO_2 molecule.

The MCP associated with the formation of RuO_3 presents a Ru−O bond lengths lying between 1.692 and 1.847 Å, and a θ(O-Ru-O) bond angle of 128.8°, slightly larger than those found in RuO_3 product. On the contrary, the N−O bond length 0.368 Å shorter than the NO equilibrium distance. These geometrical changes are induced by the highly covalent bond between O_{RuO_3} and N atoms with a length of 1.693 Å, that stabilizes RuO_3 and NO within MCP species. The analysis of the spin density reflected a chemisorbed like structure (Fig.S2b of the ESI), within a monodentate NO_2 terminal, similar to the formed $(MO_2)NO_2$ chemisorbed species in Lee *et al.*'s work [43].

The TS(3) connecting the MCR and MCP was found with an imaginary frequency of 477i cm^{-1}, within a terminal nitrate bidentate like structure. The pro and post-reactants are found energetically more stable than the associated reactants and products, as shown in Fig. 3: the MCR complex lies $\sim$ 48 kJ mol^{-1} below the reactants, while the MCP one is $\sim$ 17 kJ mol^{-1} below the products. This confirms that the identified TS(3) is

the transient species leading to the formation of RuO_3 and NO species from the reaction between RuO_2 and NO_2 compounds. However, the TS barrier is larger by about 20 kJ mol^{-1} than the one in reaction 1, with N_2O species. This implies that this reaction will be energetically less favorable at 0 K. This finding is comforted by $(N-O)_{N_2O}$ and $(N-O)_{NO_2}$ binding energies of -167.63 and -306.3 kJ mol^{-1}, respectively, obtained using $\Delta_r E(0\ K)$ of $NO_2 = NO + O$ and $N_2O = N_2 + O$, respectively, computed from the NIST standard values [41].

For the formation of RuO_4 in reaction 4, the two reactions paths explored both involve two-step mechanisms. In the reaction path 1, the connection of MCR(4-P1) to intermediate RuO_2NO_3 species by TS1(4-P1) corresponds to the formation of a ring-like structure between N, O_{NO_2}, Ru, and O_{RuO_3} atoms. The molecular complex RuO_2NO_3, which involves a nitrogen trioxide combined with a ruthenium dioxide, reveals geometric parameters for N−O bond length (1.198 Å) and O-N-O bond angle (132.2°), smaller than their counterparts in NO_3 (1.238 Å and 120°, respectively [42]), and closer to those featured in NO_2. The analysis of the MCR(4-P1) spin density reveals a physisorbed-like structure (See Fig.S3a of the ESI), with the spin density localized on NO_2, unlike the intermediate species RuO_2NO_3 (See Fig S3b of the ESI) in which the NO_2 transfers its spin density to the Ru-oxide and binds to it in a monodentate fashion. A similar result was found for adsorbed NO_2 species onto MO_3 trioxide clusters, with M=Cr and Mo [43]. Although the MCP(4-P1) portrayed a physisorbed like structure, within a terminal monodentate NO_2 structure (Fig.S4c), and a spin density localized onto the Ru metal oxide.

In reaction path 2, the TS1(4-P2) ensures the bonding between O_{NO_2} and the Ru metallic center of RuO_3, to form the intermediate species RuO_3NO_2. The latter complex exhibits Ru-O and N-O bond lengths slightly longer to those computed in RuO_3 and NO_2. In MCR(4-P2), the spin density (See Fig. S4a of the ESI) is localized on the Ru-O unit, differing from the physisorbed molecular reactant species of path-1. This chemisorbed character could explain that this reactive molecular complex species lies 58.5 kJ mol^{-1} below the reactant fragments, as well as the TS1(4-P2) barrier, which is the highest barrier in reaction path 2, but above the MCR(4-P2) by 19.3 kJ mol^{-1}. This transition state leads to the formation of the intermediate chemisorbed species RuO_3NO_2 (Fig.S4b), within a terminal monodentate NO_2 structure, slightly higher in energy than the MCR(4-P2).

For the second step of the reaction mechanism, the breaking of the symmetric bonds between $O_{RuO_3}-N$, and $Ru-O_{NO_2}$, the shrinkage of Ru−O bonds, and finally the elongation of Ru−N bond distance, is ensured by TS2(4-P2), to form the $RuO_4\cdots NO$ product complex. This MCP species portrayed a physisorbed like shape, as the spin density is localized on NO_2 (See Fig. S4c of the ESI). In addition, the MCP(4-P2) species has θ(O-Ru-O)(∼108.7°) and r(Ru−O)(∼1.702 Å) values close to those of the RuO_4 product. This MCP is geometrically different from the one identified for the path 1 (MCP(4-P1)), which had larger θ(O-Ru-O)(∼105.7°) and r(Ru-O)(∼1.714 Å) values. These geometrical characteristics are corroborated by the computed relative energies at 0 K of the MCPs, that lie 37 and 7.1 kJ mol^{-1} above the products for MCP(4-P1) and MCP(4-P2), respectively. It should be noticed that the MCP(4-P2) relative energy of -72.4 kJ mol^{-1} is in the range of calculated adsorption enthalpies from Lee *et al.*'s work [43] for group VI metal trioxide nanoclusters (from -206.8 kJ mol^{-1} (($CriO_3$)NO_2, terminal bidentate nitrate like structure) to -70.3 kJ mol^{-1}(($CriO_3$)NO_2, terminal bidentate NO_2 like structure), comforting the appropriateness of proposed reaction pathway. In addition, the highest TS2(4-P1) barrier has a relative energy with respect to the reactants equal to 48.1 kJ mol^{-1}, twice as small as those determined in reaction (2).

In conclusion, the reaction (4) path 2 is the most energetically favorable one to form RuO_4, in contrast to the thermodynamic calculations of the reaction Gibbs free energies [13], which suggested that the reaction with nitrous oxide should be more spontaneous than the one with nitrogen oxide. The kinetic parameters of these reaction pathways are investigated in following section.

Kinetic Parameters

The calculations of the temperature dependence of the rate constants have been performed at the CCSD(T)/CBS//TPSSh-5%HF/aVTZ for the reactions with N_2O and NO_2, whose values are reported in Table VI. For the formation of RuO_4 by NO_2 oxidation of RuO_3, we considered that the formation of the molecular complex reactant will be the most limiting step, especially with increasing temperature. However, in our temperature range of interest it is likely that the MCR will be formed thus we approximate RuO_4 as a fast reaction. The rate constants for N_2O and NO_2 oxidation processes were fitted with the Arrhenius equation:

$$k(T) = B \times T^n \exp(-E_a/RT), \tag{6}$$

where R is the gas constant and T is the temperature. The Arrhenius parameters are the activation energy E_a, the pre-exponential factor, B, and unit less n. The Arrhenius parameters adjusted to eq. 6 are given in Table VII. The computed rate constants related to the formation of RuO_3 through the oxidation of RuO_2 by N_2O, range from 10^{-16} at 250 K to 10^{-12} cm^3 molecule^{-1} s^{-1} at 1500 K. The oxidation of RuO_2 by NO_2 shows a similar temperature behavior, with values varying from 10^{-22} to 10^{-15} cm^3 molecule^{-1} s^{-1}. These two sets of results indicated that the mechanism involving the nitrogen dioxide is slightly slower than the one with the nitrous oxide,

TABLE VI: Rate constants in $cm^3\,molecule^{-1}\,s^{-1}$, calculated at the CCSD(T)/CBS//TPSSh-5%HF/aVTZ level of theory.

Reactions	Temperature (K)							
	250	300	400	600	800	1000	1300	1500
Formation of RuO_3								
$RuO_2 + N_2O \longrightarrow RuO_3 + N_2$	3.50×10^{-16}	1.08×10^{-15}	5.30×10^{-15}	3.75×10^{-14}	1.29×10^{-13}	3.12×10^{-13}	8.28×10^{-13}	1.37×10^{-12}
$RuO_2 + NO_2 \longrightarrow RuO_3 + NO$	2.22×10^{-22}	3.53×10^{-21}	6.20×10^{-20}	6.79×10^{-18}	6.40×10^{-17}	2.88×10^{-16}	1.38×10^{-15}	3.00×10^{-15}
Formation of RuO_4								
$RuO_3 + N_2O \longrightarrow RuO_4 + N_2$	1.07×10^{-37}	8.86×10^{-34}	8.16×10^{-29}	1.05×10^{-23}	4.77×10^{-21}	2.16×10^{-19}	8.48×10^{-18}	4.65×10^{-17}

confirming the reactions coordinates curves depicted in Fig. 3, reflecting the fact that the TS barrier is larger by $\sim$20 kJ mol^{-1} in reaction 3 than in reaction 1.

The reaction process involving the oxidation of RuO_3 by N_2O (reaction 2) appears quite slow at our temperature scale, with rate constant values varying from 10^{-37} at 250 K to 10^{-17} $cm^3\,molecule^{-1}\,s^{-1}$ at 1500 K. These values are consistent with the TS barrier displayed in Fig. 2, and emphasizing the fact that the reaction 4 involving nitrous oxide, path 2, is the more likely pathway to form RuO_4, the kinetically limiting step might only reside from the MCR complex to overcome the TS1 barrier, as the MCR complex lies energetically below the reactants at 0K.

Theoretical Results Compared to Experimental Tests

We can now discuss our theoretical results in the light of experimental data. In the framework of the VTT program [17, 44], previously described in the introduction, the ruthenium transport under humid atmospheres, and humid atmospheres with air radiolysis products precursors, with different temperature gradients was studied. Table VIII summarizes the results reported in Kajan's thesis [17].

With an atmosphere containing 50 ppmV of NO_2, the transport of ruthenium tetroxide increased by 92% at 1300 K and 42% at 1500 K, by comparison to humid air atmospheres. The increase of RuO_4 fractions was attributed to the reaction between NO_2 and RuO_3, as expressed:

$$RuO_3 + NO_2 \longrightarrow RuO_4 + NO. \quad (7)$$

The equilibrium constants K_{eq} calculated by Kajan *et al.* [17] were derived using HSC 5.11 chemistry software [45], equal to 28.55, 16.85 and 11.3 at 1300, 1500 and 1700 K, respectively.

Our equilibrium constants obtained from the kinetic reactions rate constants calculations appeared in good agreement with the ones derived from Kajan work's, though they come out slightly lower, 23.64, 9.37 and 4.66 at 1300, 1500 and 1700 K, respectively. These differences could be explained by the small deviations at higher temperatures of our derived thermodynamic properties for Ru oxides, as discussed in our previous work [12]. The decreasing amount of detected gaseous fraction of Ru as temperature increases can be attributed to the decomposition of NO_2 with temperature [46, 47]. This is fully supported by the free-energy calculations obtained for the formation of RuO_4 through nitrogen oxidation that shows higher values when temperature increases. At this stage, it is not clear how the decrease of aerosol formation is linked to the reaction of nitrogen oxide to form RuO_4. Such aspects are investigated through the study of the nucleation process of Ru dimer in a parallel work [48].

With an atmosphere containing 50 ppmV of N_2O, the experimental tests showcased a similar production of RuO_4 gaseous fraction in comparison to pure humid air atmosphere, along with a slight increase as the temperatures rise. These observations are also consistent with our quantum chemical data, as the reaction barrier in the oxidation process of RuO_3 by N_2O to form RuO_4 is large.

Altogether, this discussion leads us to conclude that the calculated kinetic rates for the formation of RuO_4 in air radiolysis products atmospheres are fully consistent with experimental observations, even if some other phenomena can play a role like surface interactions.

CONCLUSIONS

The mechanisms and kinetics of the chemical reactions leading to the formation of RuO_3 and RuO_4 gaseous species under severe accident (SA) conditions of a nuclear power plant (NPP) were elucidated by state-of-the art quantum chemical approaches. An in-depth investigation of the reaction pathways involving two air radiolysis products N_2O and NO_2 to form RuO_4 and RuO_3, following experimental observations, was conducted. The coupled-cluster theory was then employed to compute the potential energies. The transition states obtained for the formation of RuO_4 from NO_2 oxidation appeared energetically lower than the reactants.

The derivation of the related kinetic rates to form RuO_4 through the nitroxide species revealed that

TABLE VII: Arrhenius parameters calculated over the temperature range 250–2500 K from energy profiles calculated at the CCSD(T)/CBS//TPSSh-5%HF/aVTZ level of theory.

	B (cm^3 $molecule^{-1}$ s^{-1})	n	E_a (kJ mol^{-1})	k(298 K) (cm^3 $molecule^{-1}$ s^{-1})
Formation of RuO_3				
$RuO_2 + N_2O \longrightarrow RuO_3 + N_2$	2.21×10^{-21}	2.85	8.0	9.79×10^{-16}
$RuO_2 + NO_2 \longrightarrow RuO_3 + NO$	4.01×10^{-24}	3.09	27.1	3.22×10^{-21}
Formation of RuO_4				
$RuO_3 + N_2O \longrightarrow RuO_4 + N_2$	5.23×10^{-22}	2.72	106.4	6.14×10^{-34}

TABLE VIII: Measurement of transported Ru fraction in function of carrier gas and temperature in VTT tests [17]. The model primary circuit is made of either stainless steel tube or alumina tube samples. The temperature gradients range from 1300, 1500 and 1700 K down to ca. 300 K

Atmosphere (T)	Ru released rate (mg min^{-1})	Transported $RuO_{2(s)}$ (% Ru released)	Transported $RuO_{4(g)}$ (% Ru released)
Humid Air (1300 K)	0.3 ± 0.0	9.1 ± 0.5	0.0 ± 0.0
Humid Air (1500 K)	3.2 ± 0.2	12.8 ± 0.6	0.0 ± 0.0
Humid Air (1700 K)	20.3 ± 1.0	14.3 ± 0.7	0.0 ± 0.0
Humid Air + NO_2 (1300 K)	0.3 ± 0.0	0.0 ± 0.0	13.9 ± 0.7
Humid Air + NO_2 (1500 K)	3.2 ± 0.2	4.0 ± 0.2	9.9 ± 0.5
Humid Air + NO_2 (1700 K)	20.3 ± 1.0	20.2 ± 1.0	0.0 ± 0.0
Humid Air + N_2O (1300 K)	0.3 ± 0.0	6.0 ± 0.3	0.1 ± 0.0
Humid Air + N_2O (1500 K)	3.2 ± 0.3	25.4 ± 1.7	0.1 ± 0.0
Humid Air + N_2O (1700 K)	20.3 ± 1.0	15.5 ± 0.8[a]	0.0 ± 0.0[a]

[a] measured for $T = 1570$ K

nitrogen oxide process is a faster mechanism than the one involving nitrous oxide, thus contrasting the thermodynamic predictions. These results are consistent with the experimental observations and measurements acquired by the VTT program, which concluded to an increase of transported Ru gaseous fraction in humid atmospheres with air radiolysis precursors.

ACKNOWLEDGEMENTS

The computer time for part of the theoretical calculations was kindly provided by the Centre Régional Informatique et d'Applications Numériques de Normandie (CRIANN) of the University of Lille, and the HPC resources from GENCI-cines (grant 2015-project number x2015086731). This work has been supported by the French government through the Program "Investissement d'avenir" (LABEX CaPPA / ANR-11-LABX-0005-01 and I-SITE ULNE / ANR-16-IDEX-0004 ULNE), as well as by the Ministry of Higher Education and Research, Hauts de France council and European Regional Development Fund (ERDF) through the Contrat de Projets État-Région (CPER CLIMIBIO). The authors declare no competing financial interest.

AUTHOR CONTRIBUTIONS

Dr. Faoulat Miradji: conceptualization, methodology, quantum chemical calculations, kinetics calculations, data analysis, data validation, writing (original draft), writing (review & editing), visualization. Dr. Sidi M. O. Souvi: conceptualization, methodology, data analysis, data validation, writing (review & editing). Dr. Laurent Cantrel: conceptualization, methodology, data analysis, data validation writing (review & editing). Dr. Florent Louis: conceptualization, methodology, data analysis, data validation, writing (review & editing). Dr. Valérie Vallet: conceptualization, methodology, quantum chemical calculations, data analysis, data validation, writing (original draft), writing (review & editing).

[1] *Clefs CEA N°48 : Radiological and Chemical Toxicology* (Commissariat à l'énergie atomique (CEA), Paris, France, 2003).

[2] J.-P. V. Dorsselaere, A. Auvinen, D. Beraha, P. Chatelard, L. Herranz, C. Journeau, W. Klein-Hessling, I. Kljenak, A. Miassoedov, S. Paci, and R. Zeyen, Recent severe accident research synthesis of the major outcomes from the sarnet network, Nucl. Eng. Des. **291**, 19 (2015).

[3] Y. Pontillon and G. Ducros, Behaviour of fission products under severe pwr accident conditions. the vercor experimental programme—part 3: Release of low-volatile fission products and actinides, Nucl. Eng. Des. **240**, 1867 (2010).

[4] IRSN, Detection in october 2017 of ruthenium 106 in france and in europe: Results of irsn's investigations, www.irsn.fr (), online; accessed 30-June-2021.

[5] IRSN, Detection in october 2017 of ruthenium 106 in france and in europe: Results of irsn's investigations-update of information report of november 9, 2017, www.irsn.fr (), online; accessed 30-June-2021.

[6] T. Kärkelä, N. Vér, T. Haste, N. Davidovich, J. Pyykönen, and L. Cantrel, Transport of ruthenium in primary circuit conditions during a severe NPP accident, Ann. Nucl. Energy **74**, 173 (2014).

[7] M. N. Ohnet, O. Leroy, and A. S. Mamede, Ruthenium behavior in the reactor cooling system in case of a pwr severe accident, J Radioanal. Nucl. Chem. **316**, 161 (2018).

[8] F. G. Di Lemma, J. Y. Colle, O. Benes, and R. J. M. Konings, A separate effect study of the influence of metallic fission products on csi radioactive release from nuclear fuel, J. Nucl. Mater. **465**, 499 (2015).

[9] F. Miradji, F. Cousin, S. Souvi, V. Vallet, J. Denis, V. Tanchoux, and L. Cantrel, Modelling of ru behaviour in oxidative accident conditions and first source term assessments, in *The 7th European Review Meeting on Severe Accident Research (ERMSAR 2015), Marseille, France, March 24-26* (2015).

[10] P. Nerisson, H. Hu, J. F. Paul, L. Cantrel, and C. Vesin, Filtration tests of gaseous ruthenium tetroxide by sand bed and metallic filters, J. Radioanal. Nucl. Chem. **321**, 591 (2019).

[11] F. Miradji, S. Souvi, L. Cantrel, F. Louis, and V. Vallet, Thermodynamic properties of gaseous ruthenium species, J. Phys. Chem. A **119**, 4961 (2015).

[12] F. Miradji, F. Virot, S. Souvi, L. Cantrel, F. Louis, and V. Vallet, Thermochemistry of ruthenium oxyhydroxide species and their impact on volatile speciations in severe nuclear accident conditions, J. Phys. Chem. A **120**, 606 (2016).

[13] F. Miradji, *Quantum Modelling of Ruthenium Chemistry in the field of Nuclear Power Plant Safety*, Ph.D. thesis, University of Lille, Lille, France (2016).

[14] B. Clément and B. Simondi-Teissere, Stem: An irsn project on source term evaluation and mitigation, Am. Nucl. Soc. **103**, 475 (2010).

[15] NEA source term evaluation and mitigation (stem) project (2015).

[16] I. Kajan, *Transport and containment chemistry of ruthenium under severe accident conditions in a nuclear power plant*, Ph.D. thesis, Chalmers University of technology, Gothenburg, Sweden (2016), chalmers University of technology, Gothenburg, Sweden.

[17] I. Kajan, T. Kärkelä, A. Auvinen, and C. Ekberg, *ATR-2 Part A: Ruthenium chemistry and transport in a RCS due to air radiolysis products*, Tech. Rep. NKS-371 (Nordic nuclear safety research, 2016).

[18] R. A. Graham and H. S. Johnston, The photochemistry of the nitrate radical and the kinetics of the nitrogen pentoxide-ozone system, J. Phys. Chem. **82**, 254 (1978).

[19] N. Girault and L. Cantrel, *Proposition d'étude expérimentale de la radiolyse de l'air et son interaction avec la chimie de l'iode en phase gaz*, Tech. Rep. (2002) programme PARIS, Note technique IRSN 02-05.

[20] J. Tao, J. P. Perdew, V. N. Staroverov, and G. E. Scuseria, Climbing the density functional ladder: Nonempirical meta-generalized gradient approximation designed for molecules and solids, Phys. Rev. Lett. **91**, 146401 (2003).

[21] T. H. Dunning, Jr., Gaussian basis sets for use in correlated molecular calculations. i. the atoms boron through neon and hydrogen, J. Chem. Phys. **90**, 1007 (1989).

[22] K. A. Peterson, D. Figgen, M. Dolg, and H. Stoll, Energy-consistent relativistic pseudopotentials and correlation consistent basis sets for the 4*d* elements Y–Pd, J. Chem. Phys. **126**, 124104 (2007).

[23] M. J. Frisch, G. W. Trucks, H. B. Schlegel, G. E. Scuseria, M. A. Robb, J. R. Cheeseman, G. Scalmani, V. Barone, B. Mennucci, G. A. Petersson, H. Nakatsuji, M. Caricato, X. Li, H. P. Hratchian, A. F. Izmaylov, J. Bloino, G. Zheng, J. L. Sonnenberg, M. Hada, M. Ehara, K. Toyota, R. Fukuda, J. Hasegawa, M. Ishida, T. Nakajima, Y. Honda, O. Kitao, H. Nakai, T. Vreven, J. A. Montgomery, Jr., J. E. Peralta, F. Ogliaro, M. Bearpark, J. J. Heyd, E. Brothers, K. N. Kudin, V. N. Staroverov, R. Kobayashi, J. Normand, K. Raghavachari, A. Rendell, J. C. Burant, S. S. Iyengar, J. Tomasi, M. Cossi, N. Rega, J. M. Millam, M. Klene, J. E. Knox, J. B. Cross, V. Bakken, C. Adamo, J. Jaramillo, R. Gomperts, R. E. Stratmann, O. Yazyev, A. J. Austin, R. Cammi, C. Pomelli, J. W. Ochterski, R. L. Martin, K. Morokuma, V. G. Zakrzewski, G. A. Voth, P. Salvador, J. J. Dannenberg, S. Dapprich, A. D. Daniels, Farkas, J. B. Foresman, J. V. Ortiz, J. Cioslowski, and D. J. Fox, Gaussian 09 Revision C.01 (2009), gaussian Inc. Wallingford CT.

[24] P. J. Knowles, C. Hampel, and H.-J. Werner, Coupled cluster theory for high spin, open shell reference wave functions, J. Chem. Phys. **99**, 5219 (1993).

[25] P. J. Knowles, C. Hampel, and H.-J. Werner, Erratum: "coupled cluster theory for high spin, open shell reference wave functions", J. Chem. Phys. **112**, 3106 (2000).

[26] H.-J. Werner, P. J. Knowles, G. Knizia, F. R. Manby, and M. Schütz, Molpro: a general-purpose quantum chemistry program package, WIREs Comput Mol Sci **2**, 242 (2012).

[27] H.-J. Werner, P. J. Knowles, G. Knizia, F. R. Manby, M. Schütz, P. Celani, W. Györffy, D. Kats, T. Korona, R. Lindh, A. Mitrushenkov, G. Rauhut, K. R. Shamasundar, T. B. Adler, R. D. Amos, A. Bernhardsson, A. Berning, D. L. Cooper, M. J. O. Deegan, A. J. Dobbyn, F. Eckert, E. Goll, C. Hampel, A. Hesselmann, G. Hetzer, T. Hrenar, G. Jansen, C. Köppl, Y. Liu, A. W. Lloyd, R. A. Mata, A. J. May, S. J. McNicholas, W. Meyer, M. E. Mura, A. Nicklass, D. P. O'Neill, P. Palmieri, K. Pflüger, R. Pitzer, M. Reiher, T. Shiozaki, H. Stoll, A. J. Stone, R. Tarroni, T. Thorsteinsson, and M. Wang, Molpro, version 2015.1, a package of ab initio programs (2015), see http://www.molpro.net.

[28] D. Feller, Application of systematic sequences of wave functions to water dimer, J. Chem. Phys. **96**, 6104 (1992).

[29] D. Feller, The use of systematic sequences of wave functions for estimating the complete basis set, full configuration interaction limit in water, J. Chem. Phys. **98**, 7059 (1993).

[30] T. Helgaker, W. Klopper, H. Koch, and J. Noga, Basis-set convergence of correlated calculations on water, J. Chem. Phys. **106**, 9639 (1997).

[31] Z. Fang, M. A. Outlaw, and D. A. Dixon, Electronic structures of small $(RuO_2)_n$ (n = 1–4) nanoclusters and their anions and the hydrolysis reactions with water, J. Phys. Chem. A **121**, 7726 (2017).

[32] S. Khanniche, F. Louis, L. Cantrel, and I. Černušák, A density functional theory and ab initio investigation of the oxidation reaction of co by io radicals, J. Phys. Chem. A **120**, 1737 (2016).

[33] H. S. Johnston, *Gas Phase Reaction Rate Theory* (The Roland Press Co.: New York, 1966).

[34] K. J. Laidler, *Theories of Chemical Reaction Rates* (McGraw-Hill: New York, 1969).

[35] R. E. Weston and H. A. Schwartz, *Chemical Kinetics* (Prentice-Hall: New York, 1972).

[36] D. Rapp, *Statistical Mechanics* (Holt, Reinhard, and Winston: New York, 1972).

[37] E. E. Nikitin, *Theory of Elementary Atomic and Molecular Processes in Gases* (Claredon Press: Oxford, 1974).

[38] E. E. Nikitin, *Kinetics and Dynamics of Elementary Gas Reactions.* (Butterworths: London, 1980).

[39] J. I. Steinfeld, J. S. Francisco, and W. L. Hase, *Chemical Kinetics and Dynamics* (Prentice-Hall: Englewood Cliffs, 1989).

[40] A. Miyoshi, Gpop software revision 2013.07.15, available from the author.

[41] F. J. Lovas, E. Tiemann, J. S. Coursey, S. A. Kotochigova, J. Chang, K. Olsen, , and R. A. Dragoset, Nist standard reference database 114 (2005).

[42] G. Herzberg, Electronic spectra and electronic structure of polyatomic molecules (1966), new York.

[43] Z. R. Lee, L. A. Flores, W. B. Copeland, J. G. Murphy, and D. A. Dixon, Reaction of NO_2 with groups iv and vi transition metal oxide clusters, J. Phys. Chem. A **124**, 9222 (2020).

[44] I. Kajan, T. Kärkelä, U. Tapper, L.-S. Johansson, M. Gouëllo, H. Ramebäck, A. Holmgren, Stina andAuvinen, and C. Ekberg, Impact of aerosols on the transport of ruthenium in the primary circuit of nuclear power plant (2015), vTT Processes, Report No. AFT/NKS-R(14)111/1, Finland.

[45] R. A, *HSC chemistry for Windows 5.11, chemical reaction and equilibrium software with extensive thermochemical database, 5.11*, Tech. Rep. (edn. Outokumpu Research Oy, Pori, 2002)).

[46] J. C. Polanyi, Erratum: Isotopic reaction rates between methyl and hydrogen, J. Chem. Phys. **24**, 493 (1956).

[47] R. E. Huffman and N. Davidson, Shock waves in chemical kinetics: The thermal decomposition of NO_2[1a], J. Am. Chem. Soc. **81**, 2311 (1959).

[48] F. Miradji, S. Souvi, L. Cantrel, F. Louis, and V. Vallet, Reactivity of ruthenium oxide dimer species by quantum chemistry, to be submitted (2021).

Supporting Information:

Reactivity of Ru oxides with air radiolysis products investigated by theoretical calculations

Faoulat Miradji,[*,†,‡,¶,§] Sidi M. O. Souvi,[†,¶] Laurent Cantrel,[†,¶] Florent Louis,[‡,¶] and Valérie Vallet[§]

†*Institut de Radioprotection et de Sûreté Nucléaire (IRSN), PSN-RES, Cadarache, St Paul Lez Durance, 13115, France*

‡*Univ. Lille, CNRS, UMR 8522 - PC2A - Physicochimie des Processus de Combustion et de l'Atmosphère, F-59000 Lille, France*

¶*Laboratoire de Recherche Commun IRSN-CNRS-Lille1 Cinétique Chimique, Combustion, Réactivité (*C^3R*), Cadarache, Saint Paul Lez Durance,13115, France*

§*Univ. Lille, CNRS, UMR 8523 - PhLAM - Physique des Lasers Atomes et Molécules, F-59000 Lille, France*

E-mail: fmiradji@protonmail.com

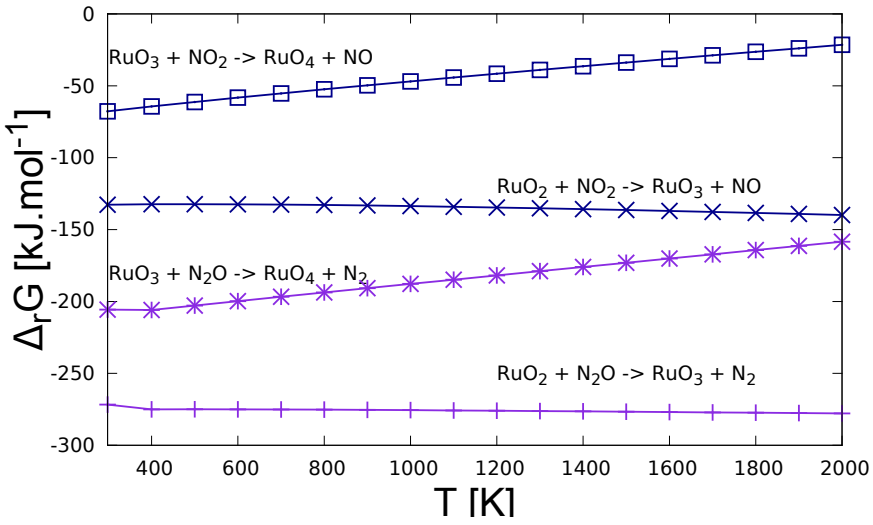

Figure S1: Gibbs energies of reaction curves of Ru oxides reactivity within N_2O and NO_2 species

Table S1: Cartesian coordinates, rotational constant, zero point energy corrections (ZPE), point group, symmetry number and frequencies (ω) of reactants and products.

Properties	RuO_2 (^1A)			RuO_3 (^1A)			RuO_4 (^1A)		
ZPE (kJ/mol)	12.73			21.28			33.46		
Rotational constants (GHZ)	X	Y	Z	X	Y	Z	X	Y	Z
	108.0097558	5.9832979	5.6692450	7.4072384	7.4072384	3.7036192	4.1428122	4.1428122	4.1428122
Full Point Group	C_2V			D_3H			T_d		
Symmetry number	4			12			24		
COORDINATES	X	Y	Z	X	Y	Z	X	Y	Z
O				0.000000	0.000000	0.000000	0.976394	0.976394	0.976394
Ru	0.000000	0.000000	0.116903	0.000000	1.686335	0.000000	0.000000	0.000000	0.000000
O	0.000000	1.624921	-0.321483	1.460409	-0.843167	0.000000	-0.976394	-0.976394	0.976394
O	0.000000	-1.624921	-0.321483	-1.460409	-0.843167	0.000000	-0.976394	0.976394	-0.976394
O							0.976394	-0.976394	-0.976394
ω_e, cm^{-1}	191.6001	962.6781	972.3287	66.2133	299.4090	299.4108	329.4897	329.4897	352.8578
				962.6525	962.6542	964.6298	352.8578	352.8578	952.782
							974.7355	974.7355	974.7355

Properties	NO_2 ($^2A_1$)			NO ($^2\Sigma$)			N_2O ($^1\Sigma$)			N_2 ($^1\Sigma_g$)		
ZPE (kJ/mol)	22.45			11.47			28.77			14.31		
Rotational constants (GHZ)	X	Y	Z	X	Y	Z	X	Y	Z	X	Y	Z
	237.9974209	12.9477411	12.2796908	0.0000000	50.9464437	50.9464437	0.0000000	12.6296066	12.6296066	0.0000000	59.9838011	59.9838011
Full Point Group	C2V			C1			C^*_v			D^*_h		
Symmetry number	4			1			4			8		
COORDINATES	X	Y	Z	X	Y	Z	X	Y	Z	X	Y	Z
N							0.000000	0.000000	-0.071636	0.000000	0.000000	0.548485
O	0.000000	1.104602	-0.142109									
N	0.000000	-1.104602	-0.142109	0.000000	0.000000	-0.614743	0.000000	0.000000	-1.199636	0.000000	0.000000	-0.548485
O	0.000000	0.000000	0.324820	0.000000	0.000000	0.537900	0.000000	0.000000	1.112364			
ω_e, cm^{-1}	750.8319	1350.6832	1652.2626	1917.78			602.8360	602.8360	1308.3437	2392.94		
							2296.36					

Table S2: Cartesian coordinates, rotational constant, zero point energy corrections (ZPE), point group, symmetry number and frequencies (ω) of intermediates complexes in the reaction (1) $RuO_2 + N_2O \longrightarrow RuO_3 + N_2$

Properties	MCR(1)			TS (1)			MCP(1)		
ZPE (kJ/mol)	43.94			37.65			36.18		
Rotational constants (GHZ)	X	Y	Z	X	Y	Z	X	Y	Z
	5.1297070	1.5161829	1.2821402	5.9809808	1.3966668	1.1766445	4.5828832	0.8077300	0.7755076
Full Point Group	C1			C1			C1		
Symmetry number	1			1			1		
COORDINATES	X	Y	Z	X	Y	Z	X	Y	Z
O	1.176175	1.577971	-0.208059	1.281787	1.542156	-0.171247	0.266574	1.447628	0.712655
Ru	0.647602	-0.000047	0.007961	0.653985	-0.000002	0.018027	0.821082	0.000086	0.052381
O	1.175012	-1.578527	-0.207531	1.281754	-1.542162	-0.171336	1.910688	0.023576	-1.232669
O	-1.288350	0.000726	0.872462	-1.184156	-0.000002	0.618028	0.293349	-1.470941	0.681997
N	-2.185310	0.000247	0.040244	-2.281084	0.000019	-0.170186	-3.448605	-0.00334	-0.328855
N	-3.100000	-0.000145	-0.612423	-3.406118	0.000000	-0.257920	-4.536038	0.002499	-0.185519
ω_e, cm^{-1}	46.4335	60.8045	135.9801	***i590.0716***	53.1052	105.0999	9.7277	11.3050	14.6701
	198.0938	237.3583	278.0440	180.1901	245.1330	275.4357	27.1644	31.7603	74.1334
	518.1889	552.8043	955.645	374.5826	420.0309	656.8689	299.9844	300.3471	962.0911
	986.0903	1127.8936	2248.4029	963.0379	986.6513	2034.3637	962.1891	964.0729	2392.3267

Table S3: Cartesian coordinates, rotational constant, zero point energy corrections (ZPE), point group, symmetry number and frequencies (ω) of intermediates complexes in the reaction (2) $RuO_3 + N_2O \longrightarrow RuO_4 + N_2$

Properties	MCR (2)			TS (2)			MCP (2)		
ZPE (kJ/mol)	50.73			49.96			48.62		
Rotational constants (GHZ)	X	Y	Z	X	Y	Z	X	Y	Z
	4.6606935	0.5272251	0.5124401	4.5094315	1.2883910	1.1932432	4.1462380	0.8012075	0.8012060
Full Point Group	C1			C1			C1		
Symmetry number	1			1			1		
COORDINATES	X	Y	Z	X	Y	Z	X	Y	Z
O	-2.077751	-1.447406	0.081334	-1.730201	1.191582	-0.502419	-2.399824	0.006821	-0.001810
Ru	-1.222062	-0.000131	-0.018906	-0.631037	-0.002725	-0.035775	-0.710126	0.000055	-0.000024
O	0.454026	-0.022183	-0.199432	-1.237449	-1.498666	0.456301	-0.143324	1.525341	-0.454124
O	-2.041450	1.469189	0.061947	1.231654	-0.522109	-0.863505	-0.153057	-0.372177	1.550811
N	3.786327	-0.000212	-0.013338	2.174776	-0.057830	-0.165012	3.311796	-0.002784	0.001148
N	3.944403	-0.010339	-1.131918	3.217841	0.215200	0.141581	4.408568	0.002171	-0.000901
O	3.622126	0.010353	1.162235	0.488162	0.706482	1.126890	-0.153419	-1.159753	-1.094963
ω_e, cm^{-1}	5.1034	9.5575	12.2012	***i572.7340***	73.7574	135.1986	10.1784	14.4004	29.4317
	25.8735	43.9646	82.1165	172.2392	222.7866	269.9064	45.0546	45.4828	330.6914
	299.3357	300.4401	602.4362	293.8226	358.2030	482.2226	330.8559	353.4842	354.8703
	03.4794	961.1501	963.0181	573.3981	810.8662	885.4292	354.9362	950.0959	971.5989
	964.9427	1308.7591	2298.3460	938.0239	942.6752	2194.1663	972.3110	972.3514	2393.2102

Table S4: Cartesian coordinates, rotational constant, zero point energy corrections (ZPE), point group, symmetry number and frequencies (ω) of intermediates complexes in the reaction (3) $RuO_2 + NO_2 \longrightarrow RuO_3 + NO$

Properties	MCR (3)			TS (3)			MCP (3)		
ZPE (kJ/mol)	46.82			39.78			38.21		
Rotational constants (GHZ)	X	Y	Z	X	Y	Z	X	Y	Z
	12.1247530	1.4050487	1.2867721	10.5644333	1.5096537	1.3601817	5.9117491	1.3365820	1.1500726
Full Point Group	C1			C1					
Symmetry number	1			1					
COORDINATES	X	Y	Z	X	Y	Z	X	Y	Z
O	2.935606	-0.005089	0.012196	2.857601	-0.016436	-0.205770	3.287999	0.000071	0.018507
N	1.747156	-0.001991	0.093568	1.782548	-0.049026	0.266331	2.254462	-0.000081	0.511212
O	0.992632	-1.080686	0.097267	0.924918	-1.101091	0.169973	1.115294	-0.000136	-0.577604
Ru	-0.751688	0.003184	-0.123102	-0.688071	0.024759	-0.123198	-0.681606	0.000008	-0.080058
O	0.997828	1.080912	0.103308	0.734797	1.183769	0.214846	-1.313479	1.514834	0.276031
O	-2.320544	-0.010906	0.382418	-2.292655	-0.159520	0.265502	-1.313632	-1.514741	0.276075
ω_e, cm^{-1}	103.2030	122.8006	171.3540	***i477.1376***	107.9314	163.6946	50.4747	104.4357	107.0845
	341.4383	367.0201	638.2001	209.5668	303.5702	429.5794	224.6151	225.7755	270.4422
	716.0601	750.6165	922.9649	551.3521	668.4614	755.6998	343.0228	518.8752	791.6028
	982.2243	1088.3080	1622.6906	858.1584	964.7844	1637.5644	955.928	977.4133	1818.5923

Table S5: Cartesian coordinates, rotational constant, zero point energy corrections (ZPE), point group, symmetry number and frequencies (ω) of intermediates complexes in the reaction (4) $RuO_3 + NO_2 \longrightarrow RuO_4 + NO$, reaction path 1

Properties	MCR (4-P1)			TS1 (4-P1)			MCP1 (4-P1)		
ZPE (kJ/mol)	44.60			47.24			53.15		
Rotational constants (GHZ)	X	Y	Z	X	Y	Z	X	Y	Z
	4.6244958	0.4907772	0.4763704	4.1110252	0.8753627	0.8486907	4.1933030	1.1058445	1.0370194
Full Point Group	C1			C1			C1		
Symmetry number	1			1			1		
COORDINATES	X	Y	Z	X	Y	Z	X	Y	Z
O	2.227767	1.402889	-0.015836	1.590395	1.484945	0.362296	1.397496	1.536232	0.292272
Ru	1.293919	-0.000626	-0.000652	0.944430	0.000005	-0.107691	0.862346	-0.000740	-0.120983
O	-0.390159	0.106043	-0.007680	-0.582562	-0.00002	-0.91454	-0.883986	-0.003585	-0.836214
O	2.043702	-1.510287	0.022653	1.590469	-1.484920	0.362244	1.395960	-1.534744	0.305205
N	-3.762405	0.320465	-0.006566	-2.450455	-0.000026	0.125042	-2.048148	0.001061	0.105676
O	-3.85663	-0.165176	-1.099835	-3.364372	0.000043	-0.628906	-3.098695	-0.005262	-0.46315
O	-3.849133	-0.110434	1.110028	-2.284144	-0.000054	1.301795	-1.761548	0.010502	1.274826
ω_e, cm^{-1}	7.4485	8.2264	9.7245	***i150.9221***	32.6407	57.5459	67.1536	84.1349	86.9353
	25.0685	37.8068	53.0252	62.8187	135.4425	231.5574	137.1682	244.0293	271.9447
	81.0845	298.0720	299.4307	261.9617	293.2727	322.2995	382.5503	468.3788	673.2463
	749.7321	962.3188	964.4556	717.9817	783.0545	955.1125	734.5048	797.5590	969.0069
	965.5071	1346.5539	1648.1523	961.6475	1309.7889	1772.9950	974.7986	1284.6279	1709.4752

Table S6: Cartesian coordinates, rotational constant, zero point energy corrections (ZPE), point group, symmetry number and frequencies (ω) of intermediates complexes in the reaction (4) $RuO_3 + NO_2 \longrightarrow RuO_4 + NO$, reaction path 1

Properties	RuO_2NO_3 (4-P1)			TS2 (4-P1)			MCP (4-P1)		
ZPE (kJ/mol)	54.16			48.00			48.32		
Rotational constants (GHZ)	X	Y	Z	X	Y	Z	X	Y	Z
	4.7439577	1.3016302	1.1812363	4.5756841	1.3969871	1.2845363	4.0632015	1.2885707	1.2304325
Full Point Group	C1			C1			C1		
Symmetry number	1			1			1		
COORDINATES	X	Y	Z	X	Y	Z	X	Y	Z
O	-1.020173	1.622270	-0.339646	1.314760	1.563326	0.046565	1.264987	1.570622	-0.000742
Ru	-0.716661	-0.016481	-0.012721	0.631369	0.015837	0.034445	0.588006	0.016582	0.000022
O	-1.850655	-1.197442	0.317747	1.604388	-1.351952	-0.187505	1.692354	-1.268250	-0.004887
O	1.144989	0.420638	1.005679	-0.910537	0.000112	-1.087939	-0.567995	-0.154289	-1.283269
N	1.836528	-0.086010	0.039374	-1.838889	-0.21623	-0.05441	-2.308117	-0.498049	0.001044
O	1.038430	-0.546600	-0.928785	-0.923399	-0.302036	1.109564	-0.559784	-0.156771	1.289184
O	3.022080	-0.132962	-0.019484	-2.948712	0.192645	-0.022523	-3.043994	0.353277	-0.001320
ω_e, cm^{-1}	33.0293	118.7055	156.040	***i662.3057***	92.3427	175.3793	70.2301	100.8289	109.6790
	190.7915	248.7800	260.5949	209.3750	217.0923	274.2974	268.4877	273.6359	302.2596
	329.2293	627.6227	745.7320,	365.2066	474.8314	505.7320	311.5653	342.8103	353.3526
	770.7360	902.6134	921.8177	605.2259	763.4506	880.7784	399.8743	833.9337	857.0257
	978.5479	1126.9111	1644.0542	928.3934	945.4573	1587.9404	951.1469	962.6116	1940.7372

Table S7: Cartesian coordinates, rotational constant, zero point energy corrections (ZPE), point group, symmetry number and frequencies (ω) of intermediates complexes in the reaction (4) $RuO_3 + NO_2 \longrightarrow RuO_4 + NO$, reaction path 2

Properties	MCR (4-P2)			TS1 (4-P2)			MCP1 (4-P2)		
ZPE (kJ/mol)	52.17			47.51			47.12		
Rotational constants (GHZ)	X	Y	Z	X	Y	Z	X	Y	Z
	3.1897811	1.9653313	1.6809660	3.3226968	1.7135198	1.5555175	3.3767902	1.5714234	1.5201628
Full Point Group	C1			C1			C1		
Symmetry number	1			1			1		
COORDINATES									
O	0.403810	0.000134	1.697715	0.359829	0.512360	-1.622831	-0.490762	-0.920366	-1.459263
Ru	0.424408	-0.000006	-0.032719	0.482317	0.040684	0.028696	-0.479087	-0.072352	0.000587
O	1.097495	1.445311	-0.572515	1.628618	-1.192603	0.161477	-1.661762	1.182711	-0.046640
O	1.097549	-1.445361	-0.572347	0.545003	1.393756	1.031210	-0.553781	-0.871274	1.485837
O	-1.499206	-1.033113	-0.124427	-2.098768	0.676576	-0.084511	2.306062	-0.625735	0.005218
N	-2.211077	-0.000016	-0.141739	-2.243018	-0.506055	0.095244	2.306671	0.552370	0.006089
O	-1.499197	1.033077	-0.124447	-1.124785	-1.171051	0.273490	1.016883	1.149275	0.006292
ω_e, cm^{-1}	112.2220	167.3905	195.6424	***i209.4966***	83.4630	114.7351	60.3839	101.3216	119.4237
	278.1602	310.6052	318.8845	151.0212	215.6688	257.5361	162.6363	255.0706	274.9627
	319.0243	331.3265	454.3623	311.8179	351.8017	431.7187	297.9400	351.7756	414.6997
	868.1649	900.0689	966.3090	854.8886	867.5116	895.9454	594.4574	808.5766	883.5150
	968.9186	1263.5710	1266.9160	936.7404	957.5014	1513.1125	953.8799	954.9926	1643.9051

Table S8: Cartesian coordinates, rotational constant, zero point energy corrections (ZPE), point group, symmetry number and frequencies (ω) of intermediates complexes in the reaction (4) $RuO_3 + NO_2 \longrightarrow RuO_4 + NO$, reaction path 2

Properties	RuO_3NO_2 (4-P2)			TS2 (4-P2)			MCP (4-P2)		
ZPE (kJ/mol)	47.37			45.61			46.19		
Rotational constants (GHz	X	Y	Z	X	Y	Z	X	Y	Z
	3.6744207	1.3620384	1.3494825	3.7315446	1.3562570	1.3505825	3.8616711	1.2054800	1.181650
Full Point Group	C1			C1			C1		
Symmetry number	1			1			1		
COORDINATES	X	Y	Z	X	Y	Z	X	Y	Z
O	2.621047	-0.421921	0.32149	2.622207	-0.478191	0.207961	2.855119	0.524763	0.020547
Ru	-0.565193	-0.003139	-0.009998	-0.554381	-0.004967	-0.006087	-0.568135	0.002717	0.000238
O	0.902222	0.764956	-0.817953	0.813932	0.914497	-0.738018	0.563461	-1.280915	-0.008644
O	-1.500292	1.222213	0.693215	0.279298	-1.060749	1.078813	0.324837	1.446432	-0.116467
O	0.198873	-0.888642	1.269538	-1.336133	-0.867055	-1.236135	-1.625903	-0.138219	-1.318681
N	2.477732	0.477794	-0.351613	2.499426	0.551009	-0.234010	2.824600	-0.610979	-0.020554
O	-1.281306	-1.077412	-1.103642	-1.517205	1.036681	0.925617	-1.464294	-0.032398	1.439918
ω_e, cm^{-1}	52.3420	107.7214	155.0084	***i229.8606***	73.5887	117.6528	24.2557	63.2794	85.7601
	181.5202	243.1397	282.7730	151.7777	215.6089	258.3733	108.9471	231.0012	281.7769
	298.2996	318.0359	329.7275	304.1770	307.1450	336.7765	319.1218	325.1197	335.4788
	613.5139	693.2790	872.3389	554.7772	672.8292	857.2355	358.5059	880.9960	932.4629
	943.0209	953.2572	1875.9435	938.2707	954.8374	1882.7888	954.5541	960.2445	1860.4660

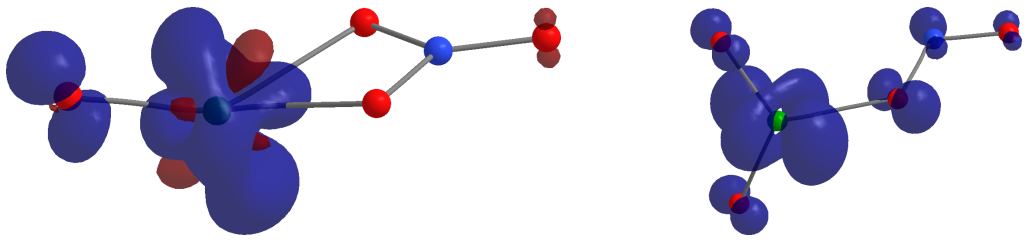

(a) (b)

Figure S2: MCR(3) (a) and MCP(3) (b) with spin density. Red atom = O, blue atom = N, green atom = Ru, blue spin density =α , and red spin density = β.

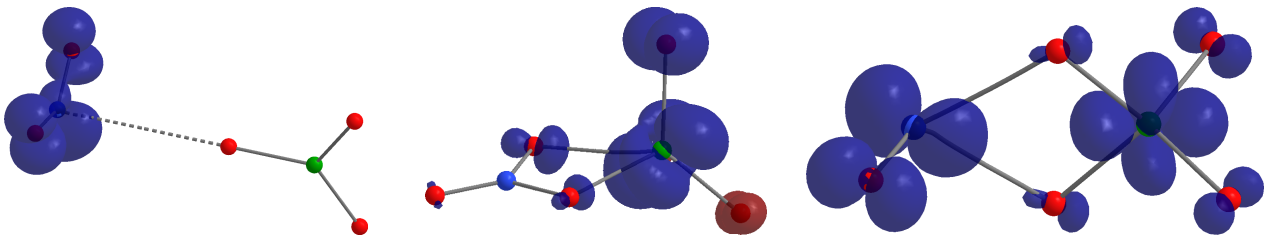

(a) (b) (c)

Figure S3: MCR(4-P1) (a), intermediate species RuO_2NO_3 (b) and MCR(4-P1) (c) with spin density. See Fig. S2 for color legend.

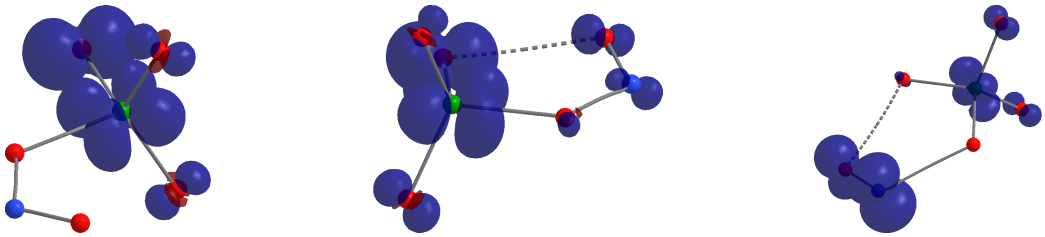

(a) (b) (c)

Figure S4: MCR(4-P2) (a), intermediate species RuO_3NO_2 (b) and MCR(4-P2) (c) with spin density. See Fig. S2 for color legend.